On the redshifts of the BL Lac 3FGL J0909.0+2310 and its close companion

D. Rosa-González,[1][*] S. Coutiño de León,[1] Y. D. Mayya,[1] A. Carramiñana,[1] I. Aretxaga,[1] J. Becerra González,[2,3] A. Furniss,[4] E. Terlevich,[1] O. Vega,[1] J. Méndez-Abreu,[5] J. León Tavares,[1] A. L. Longinotti[1] and R. Terlevich[1]

[1]*Instituto Nacional de Astrofísica, Optica y Electrónica, Tonantzintla, 72840 Puebla, Mexico*
[2]*NASA Goddard Space Flight Center, Greenbelt, MD 20771, USA*
[3]*Department of Physics and Department of Astronomy, University of Maryland, College Park, MD 20742, USA*
[4]*Physics Department, California State University East Bay, Hayward, CA 94542, USA*
[5]*School of Physics and Astronomy, University of St Andrews, North Haugh, St Andrews KY169SS, UK*

ABSTRACT

We report on the redshift of the BL Lac object 3FGL J0909.0+2310 based on observations obtained with the OSIRIS Multi-Object Spectrograph (MOS) mounted on the 10.4-m Gran Telescopio Canarias. A redshift of 0.432 ± 0.002 was obtained by the identification of three absorption features (Ca II K&H and the G band) detected in the spectrum of the BL Lac host galaxy. The closest object to the BL Lac at an angular separation of 3.8 arcsec ($\sim$21 kpc at this distance) has a similar redshift of 0.431 ± 0.002. This companion galaxy could be the most likely cause of the nuclear activity as postulated by studies based on more extended data sets and cosmological models. MOS allows us to study the object's neighbourhood within a field of view of approximately $7 \times 2 \, \text{arcmin}^2$ and we find two small groups of galaxies at redshifts 0.28 and 0.39 which are probably not related to the activity of 3FGL J0909.0+2310.

Key words: BL Lacertae objects: individual: 3FGL J0909.0+2310 – galaxies: distances and redshifts.

1 INTRODUCTION

Blazars, in particular, BL Lac objects (see Falomo, Pian & Treves 2014, for a recent review), are described as extreme active galactic nuclei (AGN) in which the relativistic jets originating close to the central massive black hole (BH) are pointing directly to the observer (Blandford & Rees 1978). The highly beamed energy released by the central BH across the entire electromagnetic spectrum makes them visible at large distances, but at the same time dilutes severely any spectral feature from its host galaxy (León-Tavares et al. 2011; Furniss et al. 2013). Shaw et al. (2013) recently compiled the largest sample of γ-ray selected BL Lac objects (BLLs) with spectroscopic redshifts. They used literature data and their own observations in 4 and 10 m class telescopes resulting in successful redshift measurements for only 44 per cent of the 475 studied BLLs.

3FGL J0909.0+2310, also named SDSS J090900.62+231112.9, (hereafter 3FGL J0909) was first detected by the National Radio Astronomy Observatory (NRAO) Green Bank telescope (Becker, White & Edwards 1991) and classified as a radio-loud AGN by Brinkmann et al. (1997). The classification as a BL Lac comes

from high-angular resolution radio images obtained with the Very Large Array of targets with detection in both the NRAO Green Bank telescope and the *ROSAT All-Sky Survey* (Laurent-Muehleisen et al. 1997). First attempts to obtain the redshift of 3FGL J0909 are from Allen et al. (2011) who, applying a non-negative matrix factorization method to the SDSS spectrum, estimated $z = 1.1844$. Aliu et al. (2012) and Shaw et al. (2013) proposed a lower limit of $z > 0.43$ based on the detection of the 2800 Å Mg II doublet in the SDSS spectrum, which could be either intrinsic, or due to the presence of absorbers in the line of sight.

3FGL J0909 appears in gamma rays in the First Catalogue of point sources detected by the *Fermi*-Large Area Telescope (*Fermi*-LAT) (1FGL; Abdo et al. 2010) with a flux in the 100 MeV to 100 GeV range of $(1.20 \pm 0.38) \times 10^{-11}$ erg s^{-1} cm^{-2}. It is also listed in the second (2FGL; Nolan et al. 2012) and third (3FGL; Acero et al. 2015) *Fermi* releases with fluxes of $1.14 \pm 0.24 \times 10^{-11}$ and $7.59 \pm 1.29 \times 10^{-12}$ erg s^{-1} cm^{-2}, respectively. These observations report a hard power-law ($\frac{dN}{dE} \propto E^{-\Gamma}$) spectral index of $\Gamma \sim 1.7$. The object is included in the First Fermi-LAT Catalogue of Sources above 10 GeV (1FHL; Ackermann et al. 2013), with a flux of $(1.00 \pm 0.50) \times 10^{-11}$ erg s^{-1} cm^{-2} and a spectral index in the 10–500 GeV energy range of $\Gamma = 1.90 \pm 0.36$. Sources with hard spectral index and detected by Fermi above 10 GeV

[*] E-mail: danrosa@inaoep.mx

are targets of interest for follow up studies at very high energies (VHE; $E > 100$ GeV). In particular, 3FGL J0909 has been observed by the imaging Cherenkov telescopes VERITAS, but only upper limits to the fluxes in the TeV regime were obtained even after 14.2 h of observation (Aliu et al. 2012). At high energies the spectral energy distribution (SED) is severely affected by the diffuse extra–Galactic background light and the appropriate corrections to recover the intrinsic spectral shape must be applied (e.g. Franceschini, Rodighiero & Vaccari 2008; Domínguez et al. 2011), before the SED can be compared with theoretical emission models (e.g. Dermer & Schlickeiser 1993; Böttcher et al. 2013). In all these studies a precise measurement of the redshift is required. It is generally assumed that BL Lac nuclei are hosted by luminous elliptical galaxies embedded in small groups of galaxies (e.g. Falomo, Melnick & Tanzi 1990; Urry et al. 2000). The presence of a close companion is usually presented as the cause of the activation of the central engine (e.g. Hopkins et al. 2008) however, *Hubble Space Telescope* observations of a large sample of BL Lac objects have shown that only around 50 per cent of them have a nearby companion finding also truly isolated BL Lac (Urry et al. 2000).

Most of the previous studies on BL Lac environment have been performed using photometric redshifts and only in a few cases (e.g. Lietzen et al. 2008; Farina et al. 2016) the environment have been characterized with spectroscopic redshifts. In this paper, we report on the distance and environment of 3FGL J0909 obtained by making use of spectroscopic redshifts gathered with the Gran Telescopio Canarias (GTC).[1]

Throughout this paper, we assume a flat cold dark matter cosmology with $\Omega_M = 0.3$ and $H_0 = 70$ km s^{-1} Mpc^{-1}.

2 OBSERVATIONS AND DATA REDUCTION

Observations were performed using the OSIRIS Multi Object Spectrograph (MOS) installed in the Nasmyth-B focus of the 10.4-m GTC under the programme GTC5−15BMEX (PI: D-RG). The observations were carried out in service mode, using the R1000R grism. The spectrum is centred at 7430 Å covering the range from 5100 to 10 000 Å at a resolution of 2.62 Å pixel^{-1} which translates to an effective resolution measured on strong sky lines of 10.86 Å. Targets are located at different positions along the dispersion axis, changing the actual wavelength coverage; the common wavelength range covered by all spectra is 5400–9500 Å.

The total observing time was divided in two observing blocks (OB) that were observed on 2016 February 6. Each OB consisted of three exposures of 1310 s on target to facilitate later removal of cosmic ray hits. The two OBs were accompanied by a common set of ancillary files that included observations of G191−B2B as a standard star, bias, flat-field and arc lamps. Both OBs were observed with air masses lower than 1.12 under *spectroscopic* cloud coverage and a seeing of 0.9 arcsec.

The data reduction was carried out by using a new MOS pipeline described in Gómez-González, Mayya & Rosa-González (2016). In short, the code reduces every MOS slit by applying the usual IRAF scripts for long slit spectra. To reduce the data, the three different target images were corrected by bias independently. Then we stacked them to obtain a single spectral image where the cosmic

rays were successfully removed. After that, every slitlet spectrum was calibrated in wavelength by using as a reference an He + Ne + Ar arc image. The dispersion solution is obtained for every single slitlet and in all the cases root-mean-square (rms) errors lower than 0.4 Å were found. This uncertainty produces a systematic error in the redshift calculations of $\sim 10^{-4}$ at a wavelength of 5000 Å.

Finally the image is calibrated in flux by using a sensitivity curve obtained by the observation of G191−B2B. The output of the pipeline is a 2D spectral image calibrated both in wavelength and flux. The final signal-to-noise ratio around 7000 Å for a point source of $r \sim 21$ mag. (e.g. MOS-35), was of around 28 in agreement with the values given by the GTC exposure time calculator for a single OB.

After analysing independently the two OBs, we noticed that – probably due to cloud coverage – one of them had about 40 per cent less counts per second than the other. The poor signal-to-noise ratio of this latter data set did not allow us to search for weak absorption lines and we do not use it in the following analysis.

MOS allows us to obtain the spectra of several objects within an effective field of view (FOV) of around 7×2 arcmin^2. Excluding the stars used as astrometric guides, within the MOS field of view, we found 71 targets brighter than $r \sim 22$. We selected our targets based on the SDSS images centred at the position of 3FGL J0909. Fifty-three of the selected targets are classified as galaxies by SDSS, four of them are unclassified (including 3FGL J0909), and the remaining 14 are classified as stars.

Given the nature of our programme, where we do not know the redshift of the source, the host galaxy morphological type, or other extra information about the surroundings, we tried to cover as many objects as possible in the OSIRIS field of view taking care of the physical limitations of the mask making procedure, giving preference to those objects classified as galaxies. Notice that some objects classified as stars could be distant galaxies, and in fact objects classified as stars by SDSS, covered by slits 25 and 35, turned out to be galaxies at $z = 0.927$ and 0.403, respectively (see Table 2). The colour–magnitude diagram (CMD; Fig. 1) shows the location of the SDSS targets where, we differentiate stars from galaxies and we marked those objects selected for spectroscopy. We cover most of the parameter space in the CMD where for SDSS galaxies brighter than $r = 21.5$, we obtain spectroscopic redshift for ~ 60 per cent of them.

Fig. 2 shows partially the slit positions on top of an *r*-band SDSS image, where we also marked the fiducial stars used for astrometry and areas free of objects used for obtaining reliable sky spectra. The length of the slits goes from 1 to 10 arcsec and the width is fixed at 1.2 arcsec. The SDSS image shows that 3FGL J0909 – in slit 21 – has a nearby companion (3.8 arcsec apart; Fig. 2) with unknown redshift, we placed one of our slits (MOS-20) on top of this source to find if it is physically associated with 3FGL J0909.

The individual spectrum for each object was extracted from the calibrated 2D spectral image by using the IRAF task APALL. In general, the extraction window is centred on the peak of the continuum, however, for the case of the extraction of the spectrum corresponding to 3FGL J0909 (MOS-21) and keeping in mind that the emission coming from the centre is featureless, we extracted the spectrum avoiding the central pixels. After trying with different apertures, we end with a final extraction window centred 3 pixels (0.75 arcsec) to the west of the continuum peak and an aperture of 4 pixels (1 arcsec). Based on the spatial profile of the emission around 5000 Å, we calculate that the central pixel contribute around

---

[1] GTC is a Spanish initiative with the participation of Mexico and the US University of Florida, and is installed at the Roque de los Muchachos in the island of La Palma.
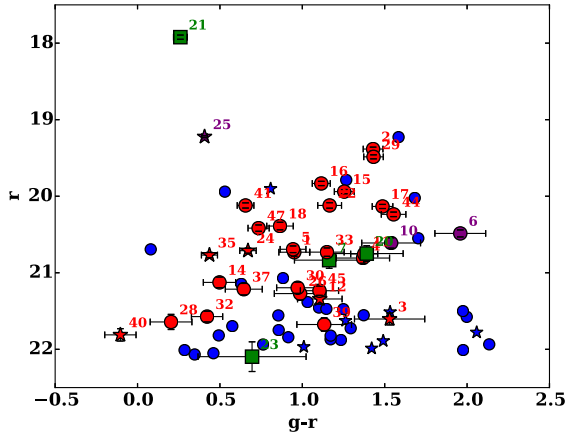
Figure 1. Colour–magnitude diagram for all objects brighter than $r \sim 22$ within the MOS field of view. The brightest object corresponds to 3FGL J0909 (MOS-21) and it is located at the top left corner of the diagram. Objects classified as stars are represented by star symbols, galaxies by circles and unidentified objects by squares. In blue are the objects in the field that we did not observe. In red, green, and purple are the targets observed by us with the slit number close to the corresponding symbol. The red symbols are for objects classified as galaxies or stars, green symbols for objects not classified by SDSS, which include 3FGL J0909 and its nearby companion (MOS-20), and purple symbols are used for targets with SDSS spectra. The QSO at redshift 0.926 (MOS-25) was classified photometrically as a star by the SDSS photometric code.

40 per cent of the light inside the aperture. Therefore by excluding that pixel from the extraction window, we improve significantly the observed equivalent widths.

In most of the cases the continuum is well detected and a fourth-order polynomial function was good enough to fit the trace along the dispersion axes. In the cases where the continuum was not well detected, we used the trace solutions found for a nearby object as reference.

Once the 1D individual spectra were extracted, we located by eye different spectral features. We looked for the most common lines observed in extra–Galactic sources, both in absorption (e.g. Ca II K&H, Mg band and NaD) and in emission (e.g. Hydrogen recombination lines, [O II] $\lambda3727$, [O III] $\lambda5007$ and [N II] $\lambda6583$). Once the lines were identified in a given spectrum, we fit a Gaussian profile which returns the position of the peaks, the integrated flux of the different lines and the equivalent widths (we used the IRAF/SPLOT command stroke k). The peaks position was used to estimate the corresponding redshifts for each individual line. The final redshift is the median of all measured values. The error is given by the standard deviation where we have more than two lines in the spectrum or the difference between the two redshift values when we have only two lines identified in the spectrum. The systematic error in redshift of 10^{-4} due to uncertainties in the wavelength calibration described in Section 2 was added in quadrature. The spectroscopic redshifts and the errors are included in Table 2. We also included the number of lines used to estimate the redshifts and if they were found in emission or in absorption.
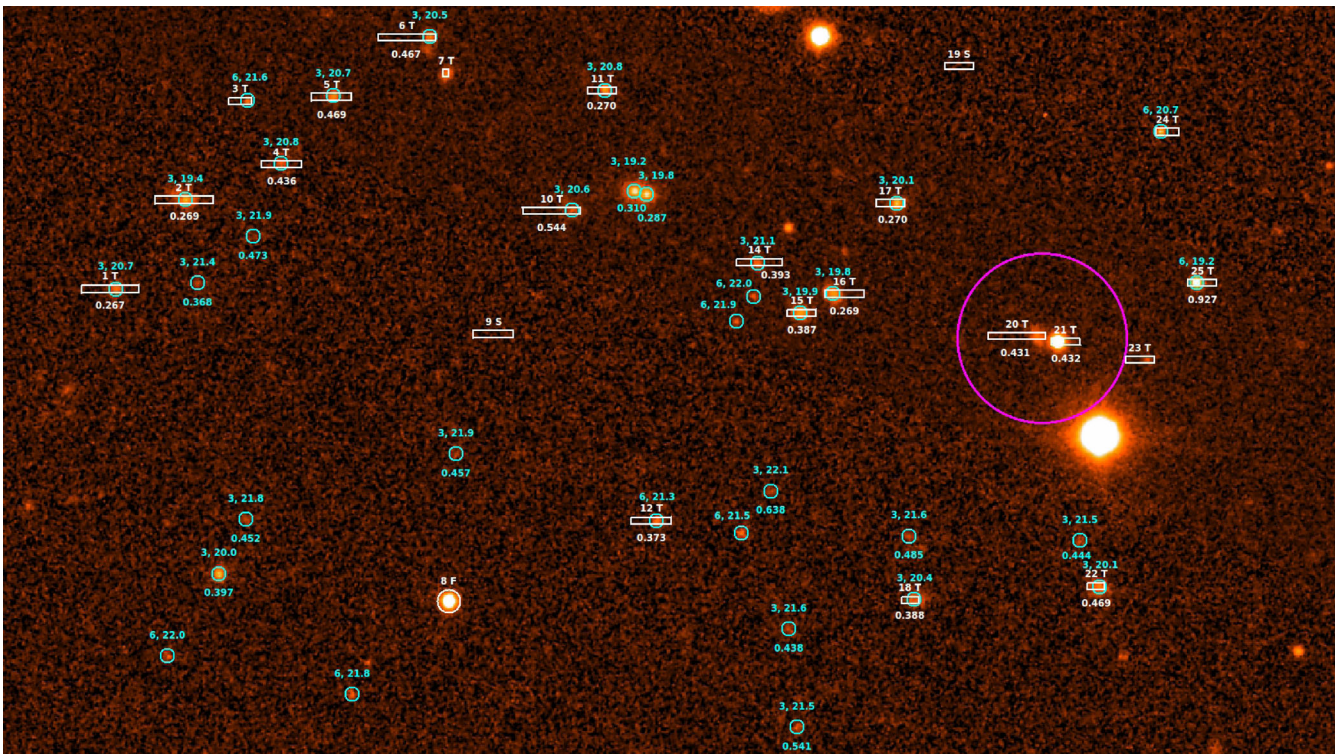
Figure 2. r-band SDSS image of an FOV of 3.9×2.2 arcmin^2 showing the position of the MOS slits (white rectangles). Above the slits are the slit numbers, and the spectroscopic redshifts are indicated below them (see Table 2). Slits 21 and 20 mark the position of 3FGL J0909 and its nearby companion, respectively, and are enclosed by a purple circle of 15 arcsec in radius. Slits 9 and 19 were used for sky spectra, and slit 8 was on top of a star used as astrometric guide. Cyan circles show the positions of SDSS objects; SDSS classification (three for galaxies and six for stars) and the r magnitude are shown above each one. Below we add the photometric redshift if any. We only show those targets with $18 < r < 22$. North is at the top and east to the left, and the FOV covers only one of the OSIRIS CCDs.
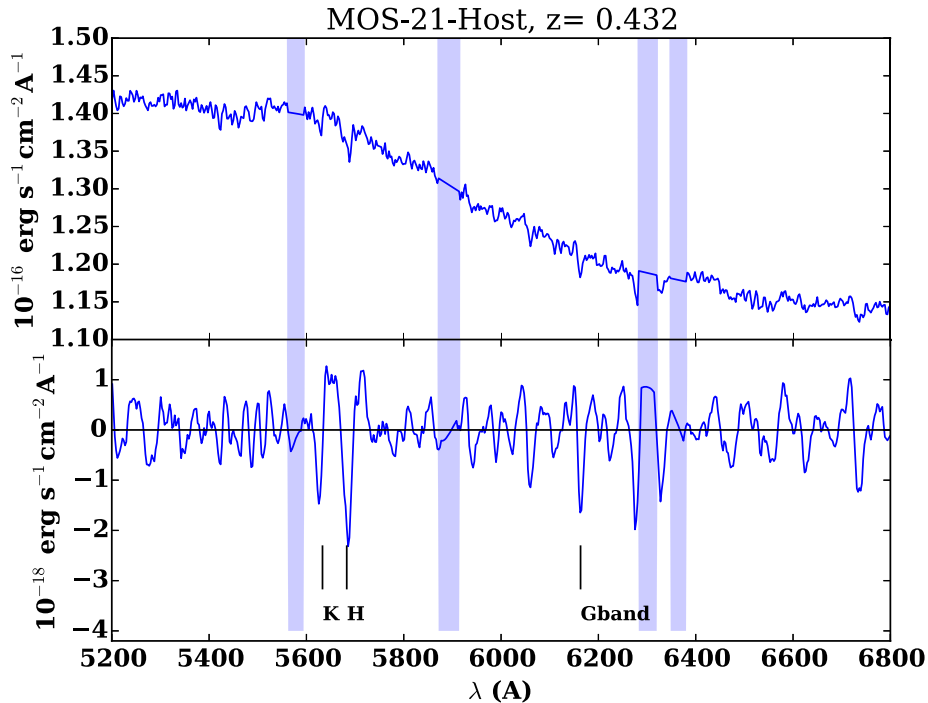
Figure 3. The observed spectrum of 3FGL J0909 host galaxy is presented in the top panel, and the continuum subtracted spectrum together with the spectral features used to obtain the redshift is in the bottom one. The spectrum of the bottom panel was smoothed to see better the weak absorption lines. The areas of the spectrum where both atmospheric lines are too strong and the telluric absorption lines are located are marked with blue rectangles in the bottom panel. Only a section of the full OSIRIS spectral coverage is plotted.

3 RESULTS

3.1 Redshift of 3FGL J0909

We obtain spectroscopic redshifts for 26 of the 35 observed targets. Targets for which we cannot extract the redshift include objects close to the slit borders and those where the signal-to-noise ratio was too low to obtain any spectral feature. Table 2 lists the SDSS properties of the selected targets, the spectroscopic redshifts and distance to 3FGL J0909. The flux calibrated spectrum of the 3FGL J0909 host galaxy is plotted in Fig. 3 (top panel). Around 5700 Å, the spectrum has a rms noise of $\sim 1.1 \times 10^{-18}$ erg s^{-1} cm^{-2} Å^{-1} (signal-to-noise ratio of ~ 150) which is a factor of 9 better than that in Aliu et al. (2012) and Shaw et al. (2013). In order to see clearly the weak absorption features, we fit a six-order polynomial curve to the original spectra plus a Savitzky–Golay filter (e.g. Press et al. 1989),[2] which removes very broad spectral features due to residuals produced in the sky substraction process, and therefore they are not related with any astrophysical source. The result of that process is plotted in the bottom panel of Fig. 3. We mark in the plot three absorption lines used to obtain the redshift of $z = 0.432 \pm 0.002$. These spectral features from Ca II K&H and the *G* band have their origin in stellar atmospheres; therefore, they are coming from the 3FGL J0909 host galaxy, and not from any intervening material in the line of sight. Table 1 shows the line fluxes and equivalent widths obtained from the Gaussian profile fit. In all cases the lines were detected above 3σ level.

Table 1. Line fluxes and equivalent widths of the three absorption lines detected in the host galaxy of 3FGL J0909.

	Line flux ($\times 10^{-17}$erg s^{-1} cm^{-2} Å^{-1})	Equivalent width (Å)
Ca II K	3.46 ± 1.07	0.25 ± 0.08
Ca II H	8.63 ± 1.44	0.62 ± 0.10
G band	3.37 ± 0.94	0.28 ± 0.08

The spectra of the nearby companion are shown in Fig. 4, and based on the observed absorption lines, we obtain a $z = 0.431 \pm 0.002$. The angular separation between these two sources is of 3.8 arcsec, which corresponds to ~ 21 kpc at the redshift of BL Lac.

We calculate the radial velocity dispersion distribution taking as reference the recessional velocity of 3FGL J0909 (Fig. 5). The distribution includes both photometric and spectroscopic redshifts. The spectroscopic data comes from our MOS observations and the photometric redshifts were obtained from the SDSS Data Release 12 (Beck et al. 2016), which includes all the galaxy-type objects within the OSIRIS FOV (7×2 arcmin^2 centred in 3FGL J0909). We did not find any significant structure around 3FGL J0909. The difference between the recession velocity of 3FGL J0909 and its nearby companion is ~ 300 km s^{-1}, which is similar to the dispersion velocities observed in galaxy groups.

3.2 Redshift of galaxies in the OSIRIS FOV

To study the existence of galaxy groups within the OSIRIS FOV, we create a histogram showing the redshift distribution based on photometric and spectroscopic redshifts (Fig. 6). As shown in Fig. 5, we did not find any significant over density around 3FGL J0909, either using the spectroscopic or photometric redshifts. Within the

---

[2] The Savitzky–Golay filter is a particular type of low-pass filter. We make use of the routine provided by the SciPy organization at SciPy.org. Information of the algorithm and multiple references can be found in the SciPy pages.

Table 2. Targets observed with GTC-MOS. Columns 1 to 6 shows: slit number (ID), SDSS coordinates, type (0 unclassified, 3 for galaxies, 6 for stars), SDSS *r* band, and SDSS *g* − *r* colour. The spectroscopic redshift (*z*), its error and the number of lines (N) used for the redshift determination are given in columns 7 and 8. Column 8 also indicates whether the lines were observed in absorption (A) or in emission (E). The angular separation (*θ*) to 3FGL J0909 is in column 9. For reference, at the redshift 3FGL J0909, 1 arcsec corresponds to 5.625 kpc. The slits on fiducial stars or those used for sky measurements are not shown.

| ID	RA (º)	Dec. (º)	Type	*r* (mag)	*g* − *r* (mag)	*z*	N	*θ* (arcsec)	Comments
MOS-1	137.303 23	23.189 51	3	20.73 ± 0.05	0.95 ± 0.09	0.2670 ± 0.0002	4/E	182.4	–
MOS-2	137.299 28	23.193 89	3	19.38 ± 0.02	1.43 ± 0.06	0.269 ± 0.0010	6/A	169.0	–
MOS-3	137.296 33	23.198 40	6	21.60 ± 0.08	1.53 ± 0.21	–	–	160.3	(d)
MOS-4	137.294 08	23.195 62	3	20.81 ± 0.07	1.37 ± 0.16	0.436 ± 0.0060	2/A	151.1	–
MOS-5	137.291 40	23.198 94	3	20.69 ± 0.04	0.94 ± 0.08	0.4685 ± 0.0003	5/E	143.2	–
MOS-6	137.287 44	23.201 85	3	20.49 ± 0.05	1.96 ± 0.15	0.4665 ± 0.0003	3/A	131.5	(SDSS)
MOS-7	137.285 40	23.199 99	0	20.84 ± 0.11	1.16 ± 0.21	–	–	123.0	(e)
MOS-10	137.279 64	23.193 33	3	20.61 ± 0.07	1.54 ± 0.18	0.544 ± 0.0030	4/A	98.8	(SDSS)
MOS-11	137.276 97	23.199 24	3	20.75 ± 0.04	1.38 ± 0.08	0.27 ± 0.0080	5/A	93.6	–
MOS-12	137.274 30	23.178 11	6	21.34 ± 0.07	1.11 ± 0.14	0.373 ± 0.0030	2/E	81.5	–
MOS-14	137.268 51	23.190 81	3	21.13 ± 0.07	0.50 ± 0.10	0.3925 ± 0.0002	5/E	58.2	–
MOS-15	137.266 25	23.188 32	3	19.94 ± 0.03	1.25 ± 0.06	0.3868 ± 0.0001	4/E	49.3	–
MOS-16	137.263 97	23.189 25	3	19.83 ± 0.03	1.12 ± 0.05	0.269 ± 0.0070	4/A	41.4	–
MOS-17	137.261 50	23.193 71	3	20.13 ± 0.03	1.49 ± 0.06	0.2698 ± 0.0004	6/A	36.7	–
MOS-18	137.260 49	23.174 30	3	20.39 ± 0.05	0.86 ± 0.08	0.388 ± 0.0002	4/E	43.9	–
MOS-20	137.254 87	23.187 18	0	20.75 ± 0.10	1.39 ± 0.22	0.431 ± 0.0020	2/A	3.8	(b)
MOS-21	137.252 16	23.186 90	0	17.92 ± 0.03	0.26 ± 0.04	0.432 ± 0.0020	3/A	0.0	(a)
MOS-22	137.250 51	23.174 90	3	20.12 ± 0.04	1.17 ± 0.07	0.4692 ± 0.0004	5/EA	32.7	–
MOS-23	137.248 43	23.186 02	0	22.10 ± 0.19	0.70 ± 0.33	–	–	15.2	(c)
MOS-24	137.246 57	23.197 21	6	20.71 ± 0.03	0.67 ± 0.05	–	–	34.8	(c)
MOS-25	137.244 83	23.189 79	6	19.22 ± 0.01	0.41 ± 0.02	0.927 ± 0.0030	2/E	29.0	(SDSS)
MOS-26	137.235 55	23.168 75	3	21.27 ± 0.09	0.99 ± 0.16	0.383 ± 0.0070	3/E	78.0	–
MOS-28	137.231 18	23.173 96	3	21.64 ± 0.10	0.20 ± 0.13	–	–	84.4	(c)
MOS-29	137.228 70	23.188 17	3	19.49 ± 0.03	1.43 ± 0.06	0.384 ± 0.0010	4/E	86.1	–
MOS-30	137.224 99	23.177 38	3	21.20 ± 0.07	0.97 ± 0.13	0.32 ± 0.0030	2/A	102.6	–
MOS-32	137.220 47	23.177 73	3	21.57 ± 0.07	0.42 ± 0.09	–	–	118.2	(c)
MOS-33	137.218 64	23.184 62	3	20.73 ± 0.05	1.15 ± 0.10	0.481 ± 0.0050	3/A	122.4	–
MOS-35	137.213 41	23.180 33	6	20.77 ± 0.03	0.44 ± 0.05	0.064 ± 0.0040	2/A	142.2	–
MOS-37	137.201 16	23.175 49	3	21.21 ± 0.08	0.64 ± 0.11	0.3929 ± 0.0001	4/E	187.6	–
MOS-39	137.189 53	23.196 77	3	21.68 ± 0.09	1.13 ± 0.17	–	–	228.5	(e)
MOS-40	137.188 27	23.181 01	6	21.81 ± 0.08	-0.10 ± 0.09	–	–	232.1	(e)
MOS-41	137.185 86	23.173 41	3	20.12 ± 0.03	0.66 ± 0.05	–	–	242.9	(e)
MOS-44	137.177 82	23.184 92	3	20.24 ± 0.03	1.55 ± 0.07	0.4347 ± 0.0006	5/A	269.3	–
MOS-45	137.174 72	23.164 06	3	21.23 ± 0.06	1.10 ± 0.12	0.3856 ± 0.0002	5/E	286.8	–
MOS-47	137.168 18	23.184 64	3	20.42 ± 0.04	0.73 ± 0.06	0.3230 ± 0.0001	4/E	304.0	–

The magnitudes and colours of the SDSS unclassified objects (type = 0) were obtained by doing photometry on the SDSS images. (a) Main target; (b) a galaxy close to 3FGL J0909; (c) close to the borders, impossible to get the spectra; (d) field star; (e) no spectral features detected; and (SDSS) we agree – within the errors – with the spectroscopic redshift given by SDSS.
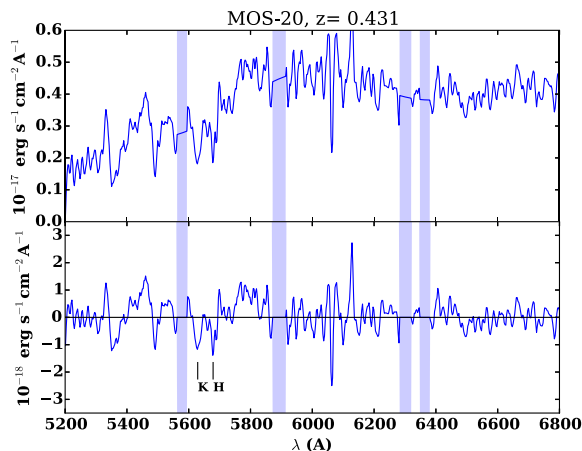
Figure 4. The spectrum of the neighbouring galaxy separated from 3FGL J0909 by 3.8 arcsec. As in Fig. 3, we marked in the bottom panel the lines used to estimate the redshift and the areas where strong sky lines are present.
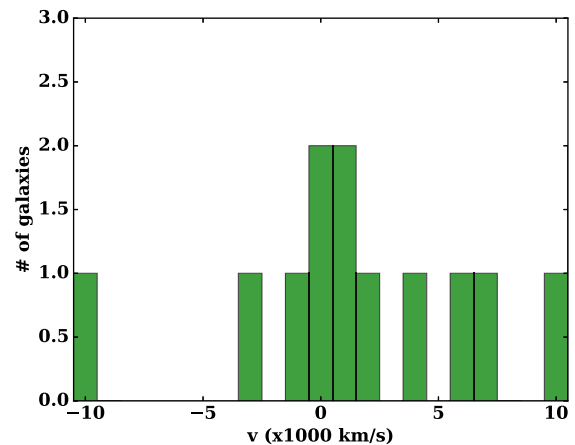
Figure 5. Radial velocity distribution taking as reference the recessional velocity of 3FGL J0909. The bin size is of 1000 km s⁻¹, and we included both spectroscopic and photometric redshifts. Only 3FGL J0909 and its close companion lie inside the central bin.
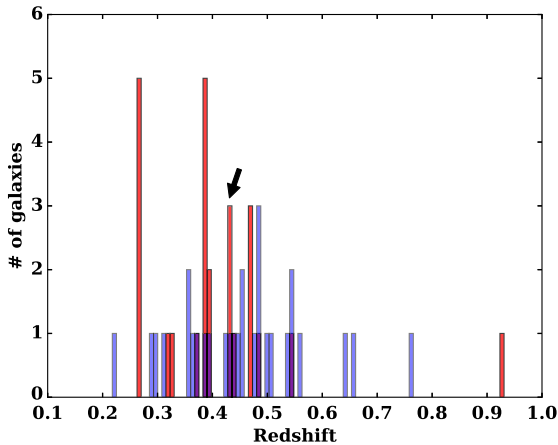
Figure 6. Spectroscopic (red) and photometric (blue) redshift distributions of the targets within the OSIRIS FOV. The bin size is 0.0075, and the bin containing 3FGL J0909 and its close companion is marked with an arrow. Two small groups of galaxies at redshifts 0.28 and 0.39 are identified.

redshift bin where 3FGL J0909 is located, we find just another galaxy (MOS-44) with a similar redshift 0.4347 ± 0.0006 but separated by $\sim$270 arcsec. This angular separation corresponds to a projected physical distance of 1.5 Mpc; therefore, this galaxy is too far away to be related to the nuclear activity of 3FGL J0909.

Two small peaks appear in the spectroscopic distributions at 0.28 and 0.39, which are not related with 3FGL J0909. The minimum and maximum distances between the members belonging to the group at $z = 0.28$ are 86 and 585 kpc, respectively. The corresponding values for the group at $z = 0.39$ are 286 kpc and 1.7 Mpc. The spectroscopic study of these two groups will be presented in a forthcoming paper.

4 CONCLUSIONS

By carefully extracting the GTC spectra of 3FGL J0909 avoiding the featureless central engine we assign a redshift of $z = 0.432 \pm 0.002$ to its host galaxy. We find a neighbouring galaxy just 21 kpc apart with similar redshift that could be the cause of the BL Lac nuclear activity observed in 3FGL J0909. In fact, the presence of nearby companions separated by tens of kpc have been observed in other BL Lac objects pointing to the possible connection between the gas fueling towards the nuclei due to a close encounter and the consequent triggering the nuclear activity (e.g. Falomo 1996; Farina et al. 2016).

Our results show that in an FOV of $7 \times 2\,\text{arcmin}^2$ exist two groups of galaxies with mean redshifts which are quite different from the spectroscopic redshift of the BL Lac. This result indicates that conclusions obtained by associating the redshift of a given object based on the presence of a galaxy group within the studied FOV (e.g. Muriel et al. 2015) must be used with caution.

The fact that we now have a precise spectroscopic redshift determination for 3FGL J0909, and taking into account that photons from this object have been detected above 10 GeV, makes 3FGL J0909 an interesting target for Cherenkov telescopes.

REFERENCES

Abdo A. A. et al., 2010, ApJS, 188, 405
Acero F. et al., 2015, ApJS, 218, 23
Ackermann M. et al., 2013, ApJS, 209, 34
Aliu E. et al., 2012, ApJ, 759, 102
Allen J. T., Hewett P. C., Maddox N., Richards G. T., Belokurov V., 2011, MNRAS, 410, 860
Beck R., Dobos L., Budavári T., Szalay A. S., Csabai I., 2016, MNRAS, 460, 1371
Becker R. H., White R. L., Edwards A. L., 1991, ApJS, 75, 1
Blandford R. D., Rees M. J., 1978, Phys. Scr., 17, 265
Böttcher M., Reimer A., Sweeney K., Prakash A., 2013, ApJ, 768, 54
Brinkmann W. et al., 1997, A&A, 323, 739
Dermer C. D., Schlickeiser R., 1993, ApJ, 416, 458
Domínguez A. et al., 2011, MNRAS, 410, 2556
Falomo R., 1996, MNRAS, 283, 241
Falomo R., Melnick J., Tanzi E. G., 1990, Nature, 345, 692
Falomo R., Pian E., Treves A., 2014, A&AR, 22, 73
Farina E. P., Fumagalli M., Decarli R., Fanidakis N., 2016, MNRAS, 455, 618
Franceschini A., Rodighiero G., Vaccari M., 2008, A&A, 487, 837
Furniss A., Fumagalli M., Danforth C., Williams D. A., Prochaska J. X., 2013, ApJ, 766, 35
Gómez-Gónzalez V. M. A., Mayya Y. D., Rosa-González D., 2016, MNRAS, 460, 1555
Hopkins P. F., Hernquist L., Cox T. J., Kereš D., 2008, ApJS, 175, 356
Laurent-Muehleisen S. A., Kollgaard R. I., Ryan P. J., Feigelson E. D., Brinkmann W., Siebert J., 1997, A&AS, 122, 235
León-Tavares J., Valtaoja E., Chavushyan V. H., Tornikoski M., Añorve C., Nieppola E., Lähteenmäki A., 2011, MNRAS, 411, 1127
Lietzen H., Nilsson K., Takalo L. O., Heinämäki P., Nurmi P., Keinänen P., Wagner S., 2008, A&A, 482, 771
Muriel H., Donzelli C., Rovero A. C., Pichel A., 2015, A&A, 574, A101
Nolan P. L. et al., 2012, ApJS, 199, 31
Press W. H., Flannery B. P., Teukolsky S. A., Vetterling W. T., 1989, Numerical Recipes in C. The Art of Scientific Computing. Cambridge Univ. Press, Cambridge
Shaw M. S. et al., 2013, ApJ, 764, 135
Urry C. M., Scarpa R., O'Dowd M., Falomo R., Pesce J. E., Treves A., 2000, ApJ, 532, 816

This paper has been typeset from a TeX/LaTeX file prepared by the author.